Diurnal Variation of Tropical Ice Cloud Microphysics: Evidence from Global Precipitation Measurement Microwave Imager (GPM-GMI) Polarimetric Measurements

Jie Gong[1], Xiping Zeng[2], Dong L. Wu[3], Xiaowen Li[4]

1. GESTAR Program, Universities Space Research Association, Columbia, MD
2. U.S. Army Research Laboratory, Adelphi, MD
3. NASA Goddard Space Flight Center, Greenbelt, MD
4. GESTAR Program, Morgan State University, Baltimore, MD

Corresponding author: Jie Gong (Jie.Gong@nasa.gov)

Key points:

1. The first study of the diurnal cycle of tropical ice cloud microphysics using spaceborne high-frequency microwave polarimetric measurements.
2. The polarimetric difference's (PD's) diurnal cycle precedes that of the ice cloud occurring frequency and total mass by about 2 hours.
3. The diurnal cycle of PD can be explained by changes of the ice crystal axial ratio using radiative transfer calculations.

24   **Abstract**

25   The diurnal variation of tropical ice clouds has been well observed and examined in terms of the

26   occurring frequency and total mass but rarely from the viewpoint of ice microphysical

27   parameters. It accounts for a large portion of uncertainties in evaluating ice clouds' role on

28   global radiation and hydrological budgets. Owing to the advantage of precession orbit design and

29   paired polarized observations at a high-frequency microwave band that is particularly sensitive to

30   ice particle microphysical properties, three years of polarimetric difference (PD) measurements

31   using the 166 GHz channel of Global Precipitation Measurement Microwave Imager (GPM-GMI)

32   are compiled to reveal a strong diurnal cycle over tropical land (30°S–30°N) with peak

33   amplitude varying up to 38%. Since the PD signal is dominantly determined by ice crystal size,

34   shape, and orientation, the diurnal cycle observed by GMI can be used to infer changes in ice

35   crystal properties. Moreover, PD change is found to lead the diurnal changes of ice cloud

36   occurring frequency and total ice mass by about 2 hours, which strongly implies that

37   understanding ice microphysics is critical to predict, infer, and model ice cloud evolution and

38   precipitation processes.

39

40   **Plain Language Summary:**

41   Along with the rising and setting of the Sun, our Earth's clouds vary between day and night. For

42   tropical ice clouds, there are many evidences showing that the cloud cover and thickness change

43   dramatically during a day (referred to as the "diurnal cycle") but few hints of what happens to

44   individual ice crystals. Using a new spaceborne satellite instrument called GPM-GMI, we found

45   that ice crystal size or shape also exhibits a strong diurnal cycle over tropical land but not over

46   tropical ocean. We can further infer that the microscopic variation of ice crystals may be an

47   important reason for the change of ice cloud cover and thickness later on.

48

49   **1. Introduction**

50   Upper tropospheric ice clouds, namely anvils and cirrus, spread to cover vast areas and persist

51   for hours to days. They are a major modulator of Earth's radiation and thus play an important

52   role in weather and climate changes (e.g., Hartmann et al., 1984; Raymond and Zeng, 2000;

53   Waliser et al., 2009). Studies have shown that the cloud radiative effect (CRE) of the clouds

54   strongly depends on physical details, such as cloud top height (Kiehl, 1994), thickness (Hong et

55   al., 2016; Hartmann and Berry, 2017), overlaying situation (Hartmann et al., 2001), and

56   microphysical properties (Liou et al., 2002; Zeng et al., 2009a, b; Tang et al., 2017). Fu and Liou

57   (1993), for example, showed that the radiative heating rate for a layer of ice cloud with a fixed

58   ice water path could differ by a factor of 10 when the mean effective radius of the ice particles

59   varies by a factor of 5. Reducing the uncertainty of CRE requires a better understanding of ice

60   cloud microphysical properties, which is essential not only to remote sensing of the bulk optical

61   properties but also to the simulation of CRE (Tang et al., 2017). In addition, ice clouds,

62   especially the anvils and mixed-phase clouds in deep convections, contribute much to tropical

63   precipitation and vertical circulations (e.g., Raymond and Zeng, 2000; Liu and Zipser, 2008).

64   Since ice clouds play a critical role in the global water and energy cycles, it is imperative to

65   determine their microphysical processes as well as their macro-characteristics.

66   One of the large variabilities of tropical ice clouds is their strong response to the diurnal

67   variation of solar heating at the Earth's surface (Yang and Slingo, 2001; Tian et al., 2004; Hong

68   et al., 2006). The diurnal variations of ice clouds have been observed using various cloud

69   properties such as occurring frequency, total mass, and cloud cover with a variety of measuring

70   techniques (e.g., Tian et al., 2004; Liu and Zipser, 2008; Eriksson et al., 2010; Millan et al., 2013;

71   Jiang et al., 2014) in conjunction with some other key atmospheric variables such as water vapor

72   (Soden, 2000), surface temperature (Dai et al., 2004) and convective activity (Chung et al., 2007).

73   These metrics have been extensively studied over the past two decades especially owing to the

74   rapid advance in spaceborne instrument technology, as well as the increase in a satellite's spatial

75   and temporal coverage. However, microphysical properties of ice crystals, such as crystal shape,

76   orientation, and size distribution, have rarely been investigated, since it is a challenge to observe

77   ice crystal microphysical properties accurately from space. Some of the integrated properties

78   (e.g., effective diameter) are derived products from primary properties, such as mass, coverage,

79   and type, in most satellite observations (e.g., CloudSat) with arbitrary assumptions. Although

80   new retrieval techniques such as one-dimensional variation method (1DVAR) and neural

81   network can retrieve all desired variables together at least theoretically, oversimplified

82   microphysical assumptions are still required in the retrieval model or training database, which

83   directly impact their outputs (e.g., Boukabara et al., 2011; Duncan and Kummerow, 2016).

84   Hence, how to observe and analyze the diurnal variation of cloud ice microphysics from space is

85   inherently a difficult yet interesting topic.

86   Polarimetric difference (PD) between paired vertically and horizontally polarized (V-pol and

87   H-pol hereafter for abbreviation) channels at a fixed incidence angle is a relatively matured

88   product and can be measured precisely from space. Recently, the polarimetric data have been

89   used to study ice microphysical properties (e.g., Skofronick-Jackson et al. 2015; Homeyer and

90   Kumjian, 2015; Hioki et al., 2016). In particular, studies of PD from passive and active

91   spaceborne measurements at visible and microwave wavelengths show that nonspherical ice

92   crystals are not randomly oriented but usually horizontally oriented (Prigent et al., 2001, 2005;

93   Davis et al., 2005, 2007; Zhou et al., 2012; Defer et al., 2014). Gong and Wu (2017) (GW17

94   hereafter) first identified the similar features from the GPM-GMI 166 and 89 GHz observations.

95   Taking advantage of GPM's precession orbit, this paper aims to better understand the diurnal

96   variation of PDs in the tropics and its implication for ice crystal's microphysical properties and

97   how they vary together with macroscopic quantities such as cloud occurring frequency and mass.

98

99   **2. Diurnal Variations of 166 GHz Polarimetric Radiance Difference**

100   The GPM core satellite has a dual-frequency precipitation radar (DPR) and a passive GMI

101   instrument with 13 channels between 10 and 190 GHz (Hou et al. 2014; Skofronick-Jackson et al.

102   2015). Among the 13 channels, the 10.65, 18.7, 36.5, 89, and 166 GHz channels have V-pol and

103   H-pol. In this study, only the 166 GHz polarization data are used because this channel is

104   sensitive to cloud ice scattering and its PD is not sensitive to water cloud emission. Furthermore,

105   the PD at this channel is least contaminated by surface polarizations in the tropics (GW17). The

106   GPM core satellite flies at the altitude of 407 km in a non-Sun-synchronized orbit that covers a

107   latitude range between 68°S and 68°N. It slowly progresses over the local solar time (LST),

108   making it ideal to study the diurnal variability of clouds and precipitation. The GMI has a

109   forward conical scan viewing geometry off-nadir at an angle of 48.5° (see Skofronick-Jackson et

110   al. 2015 for details).

111   The current study uses Version 1.4 of Level-1C inter-calibrated GMI brightness temperature

112   (TB) observations at 166 GHz during February 2014 – December 2016 (GPM X-Cal Working

113   Group, 2015). The diurnal cycle is not separated further by seasons, as the seasonality in the

114   tropics between 30°S and 30°N is small. Furthermore, since it takes approximately 45 days for

115   the GPM satellite to precess through all LSTs, integration over three years on a time interval of 2

116   hours can generate robust and useful cloud statistics. The GMI 183±3 GHz radiance is used to

117   screen the "confident cloudy-sky" scenes for estimating the cloud occurring frequency (OF) and

118   the mean cloudy-sky TB (TB_{cld}). The colder TB_{cld} is, the thicker the ice cloud is. As at 166 GHz,

119   -TB_{cld} is roughly linearly correlated with the column-integrated ice water path (IWP) as long as

120   the cloud is not completely opaque (Gong and Wu, 2014). Therefore, -TB_{cld} can be used as a

121   proxy for IWP along the GMI's line of sight. Both 166 and 183±3 GHz channels belong to the

122   high-frequency group that scans simultaneously with the same footprint size of 4.2 X 7.0 km^2.

123   The "3σ cloud detection" threshold is employed to distinguish between clear- and cloudy-sky

124   scenes, which is identical to Gong and Wu [2014; 2017]. This method first identifies the peak

125   (TB_{peak}) and standard deviation (σ) of the probability density function (PDF) of the TB

126   observations in a given region or a latitude belt over the period of interest, and then the cloudy-

127   sky scene is defined at places where TB < TB_{peak} - 3σ. In practice, this procedure is iterated twice

128   to remove the broadening effect introduced by clouds (i.e., bias in σ). Since a large amount of

129   "possible ice cloud present" scenes with relatively warmer TB is excluded using this method, OF

130   is much smaller and TB_{cld} is cold-biased. However, to fully describe the ice cloud polarization

131   feature, it is necessary to account for the polarization signal corresponding to these "warmer ice

132   cloud" scenes that are in general populated with cirrus and thin anvil clouds. Hence, another

133   threshold is proposed in the next paragraph to separate the clear-sky and cloudy-sky polarimetric

134   signatures.

135   Three years of the 166 GHz observations in the tropics (30°S-30°N) are sorted to the nearest

136   LST slot that is separated by a 2-hour interval. Then, the 2D PDF integration is performed for

137   each of the 12 LSTs according to its V-pol TB (TB_V) and PD values. PD is defined as

138 $$PD \equiv TB_V - TB_H \qquad\qquad\qquad \text{(Eqn 1)}$$

139   A positive PD implies that the upwelling microwave radiation must have a shorter cloud optical

140   length in V-pol (τ_V) than in H-pol (τ_H) due to either scattering or absorption along the path and

141   vice versa. Once the PDF is compiled, the mean and standard deviation of the PD value within

142   each TB_V bin is then calculated to draw the final curves shown in Fig. 1a for the oceanic and Fig.

143   1b for the landmasses, respectively. The cloudy-sky thresholds are drawn in the black dash lines.

144   Following GW17, the bottom-up bell curve is referred to as the "PD-TB" relationship. The same

145   as found in GW17, the TB_V value corresponded to the peak PD robustly located at approximately

146   200 K, and the broadness of the spread is strikingly similar across different LSTs. These features

147   again reveal an apparently nearly universal bell-curve in the PD-TB relationship. These curves

148   spread out at the peak PD but converge to roughly the same TB values as PD values approach

149   zero. At the warm TB end when the curves converge, another threshold (dash-dot lines) is set, to

150   the left of which is considered a full cloudy-sky PD-TB relationship. Since the dynamic range of

151   TB_v for the PD-TB relationship holds the same during a day, the curvature of the curve is solely

152   determined by its peak value of PD (PD_{peak}).

153   The PD_{peak} from tropical clouds exhibits a clear diurnal cycle over land but not over ocean.

154   The amplitude of PD_{peak} variation over land is ~ 38% and that over ocean is only ~ 6%.

155   Furthermore, the maximum and minimum of PD_{peak} occur at local morning (9:00 LST) and

156   afternoon (16:00 LST) over land, while the difference is not statistically significant over ocean.

157   The general conclusion of local morning maximum and afternoon minimum of PD_{peak} over land

158   is robust against using different time intervals (1 hr and 3 hrs), although the exact LST may vary

159   by +/- 1hr. As will be shown in the next section, PD_{peak}, or the curvature of the curve, is the key

160   variable to correspond to the column-integrated optical axial ratio.

161   The diurnal variation of PD_{peak} is better exhibited in Fig. 2a (ocean) and 2b (land) where

162   PD_{peak} clearly shows an anticorrelation with cloud occurrence frequency and mean cloud TB.

163   Compared to the diurnal cycle of upper-tropospheric clouds previously identified using Tropical

164   Rainfall Measurement Mission (TRMM)'s precipitation radar and visible and infrared scanner,

165   the diurnal cycle of PD_{peak} also anticorrelates with that of the area and cloud fraction for both

166   ocean and land surface conditions. In those analyses, over ocean, the diurnal cycle of PD_{peak}

167   precedes that of the precipitation rate (PR) by ~ 2 hrs, but for land cases, it lags the PR diurnal

168   cycle by ~ 2 hrs (reference: Fig. 7 of Hong et al., 2006; Fig. 3 of Liu and Zipser, 2008).

169   To showcase the direct correlation of the diurnal cycles between PD_{peak} and the macro-

170   quantities of the same group of clouds, Fig. 2 also displays the time series of PD_{peak}, OF, and

171   TB_{cld}. As mentioned previously, to compute the latter two variables, all cloudy-sky scenes with

172   TB below the "3σ thresholds," shown as the dashed lines in Fig. 1, are used here. In addition, to

173   remove some casual noise produced by only taking PD_{peak} values, PD from a relatively small TB

174   window ($180K < TB_V < 210K$) is averaged (referred to as $\overline{PD_{peak}}$), showing that the major

175   conclusions hold robustly against using 1 hr time interval, as well as against variations of the

176   thresholds (e.g., using dash or dash-dot lines in Fig. 1 to compute OF and TB_{cld} or using slightly

177   different windows to compute $\overline{PD_{peak}}$).

178   Similar to the findings from TRMM data, the diurnal cycle of $\overline{PD_{peak}}$ is the opposite of

179   OF and total mass (-TB_{cld}), while the latter two go together tightly. However, the largest

180   correlation coefficient is found when $\overline{PD_{peak}}$ leads the other two quantities by ~ 2 hours, when

181   the correlation coefficient exceeds -0.9. That is to say, when $\overline{PD_{peak}}$ reaches its minimum

182   (maximum) during the day, ice cloud coverage and total ice cloud mass reach their maximum

183   (minimum) within ~ 2 hrs. This is the first study implying that ice crystal microphysics may play

184   a key role on the formation/dissipation processes of ice clouds. Furthermore, this leading time of

185   2 hrs is robust against using a time interval of 1 hr, but it would be "distorted" to 3 hrs if we use

186   3 hrs as the time interval for the analysis. Such a sensitivity exercise emphasizes the importance

187   of having enough samples and small enough time steps in order to investigate the diurnal

188   variation.

189   The only exception is between $\overline{PD_{peak}}$ and OF over ocean where the correlation is the

190   largest without 5 hour advancement. This result changes with choosing different time interval so

191   it's not a roubust result. Since the diurnal cycle of $\overline{PD_{peak}}$ is too small over ocean to beat its own

192   variability (error bars on Fig. 2a), the correlation among these three cloud parameters are not

193   statistically significant over ocean anyway.

194   In summary, a strong diurnal cycle of GMI's 166 GHz PD is found for tropical ice clouds

195   over land and a much weaker diurnal cycle over the ocean. The diurnal variations of PD lead

196   those of the total ice cloud coverage and mass by ~ 2 hrs.

197

198   **3. Interpretation and Radiative Transfer Model Simulations**

199   As the observed PD is dominantly positive, by definition, ice particles in the ice cloud layer

200   must possess anisotropic characteristics in terms of the bulk microphysical properties along the

201   line of sight. In other words, the ice particles within this ice cloud layer must be aspherical

202   microphysically and, more importantly, also aspherical on an integrated sense. Previous studies

203   hence proposed that the majority of aspherical ice crystals should have oriented preferably along

204   the horizontal direction rather than randomly oriented (Prigent et al., 2001, 2005; Davis et al.,

205   2005, 2007; Zhou et al., 2012, 2013; Defer et al., 2014). GW17 too one step further that

206   explained the entire bottom-up bell curve feature of the PD-TB relationship with a conceptual

207   model. In this model, when a cloud is optically thick, both V- and H-pol radiations are saturated

208   at the same level, causing PD to diminish. By applying this hypothesis to a radiative transfer

209   model (RTM), GW17 simulated the observed PD-TB relationship for 89, 166, and 640 GHz at

210   the same time by controlling one parameter, called the "optical aspect ratio" (AR), defined as

211    $AR \equiv {\tau_V}/{\tau_H}$. The ratio is not the typical "axial ratio" parameter often used to describe the

212   eccentricity of an aspherical ice particle; it is the column integrated optical property difference

213   between V-pol and H-pol at a given frequency, in the present case, 166 GHz. Further, by

214   adjusting the value of AR, GW17 found the curvature of the PD-TB relationship changes, but the

215   warm and cold ends remain converging to 0 (as expected theoretically) at roughly the same TB_V

216   values. In other words, PD_{peak} is directly tied to the value of AR.

217   Following on the GW17 approach, the observed diurnal variation of the PD-TB relationship

218   is simulated using different AR values in the same RTM as detailed in GW17. Briefly speaking

219   about the setup, two parallel simulations are run at the same time; one with a regular extinction

220   profile and the other profile is arbitrarily multiplied by a fixed AR value. Gamma distribution is

221   employed for the particle size distribution, with the effective diameter fixed at 160 μm. By

222   varying the cloud optical depth to create the dynamic range of TB, the difference between the

223   two parallel runs creates the "PD-TB" bell curve observed (c.f., Section 4.2 of GW17). In this

224   study, AR is changed from 1.0 to 2.0 with increments of 0.02 for each set of simulation. The

225   "best-fit" AR value is then defined such that the standard deviation between the simulated PD

226   and the observed counterpart reaches minimum (see Fig. 3a). In this way, the AR value is

227   "retrieved" for different LSTs and its time series are displayed in Fig. 3b and 3c over the ocean

228   and land surfaces, respectively. This AR "retrieval" is technically similar to a standard retrieval

229   process except for no actually retrieving a physical quantity with a set of rigorous algorithms.

230   As expected, the variation of the "best-fit" AR is tightly correlated with the diurnal variation

231   of $\overline{PD_{peak}}$. When the diurnal variation amplitude is small compared to the internal variability at a

232   given LST, the "best-fit" AR is insensitive to the small change of $\overline{PD_{peak}}$. That's the case over

233   tropical ocean. On the other hand, when the tropical land convection and the associated anvil and

234   cirrus clouds start to experience the most dramatic diurnal change from noon to late night, the

235   "best-fit" AR value also changes accordingly.

236   The value of AR physically corresponds to an integrated result from a few ice microphysical

237   parameters that impact $^{\tau_V}/_{\tau_H}$ by definition. $\tau = \int_{z_{base}}^{z_{top}} \int_{D_{min}}^{D_{max}} N(D)A(D)dD\ dz$, where N is the

238   number density, A is the cross section of the particle size perpendicular to the incoming radiation,

239   D is the diameter, and z_{base} and z_{top} are the cloud base and top heights, respectively (Heymsfield

240   et al., 2003). With V-pol and H-pol detecting radiation from the surface that penetrates up

241   through the same ice cloud layer, only the aspherical particle shape and diameter at two specific

242   directions that are perpendicular to V-pol and H-pol, assuming that the 100% horizontal-

243   alignment is valid. Under this assumption, large (small) AR corresponds to high (low) axial ratio

244   of the ice particles. That means over land, the majority of ice particles tend to become more and

245   more sphere-like from morning (9 am) to afternoon (4 pm), and from then on horizontally

246   oriented non-spherical ice crystals start to dominate the PD signal again.

247   This proposed diurnal variation of ice crystal orientation is consistent with the physics model

248   of radiation-induced ice crystal growth (or the radiative effect on microphysics [(e.g., Zeng

249   2008]). In the physics model, horizontally oriented ice crystals near the cloud top, in contrast to

250   the vertically oriented ones, emit longwave radiation effectively to space, subsequently have low

251   surface temperature, and thus can grow to precipitation-sized particles, which explains the

252   positive value of the PD observed. Meanwhile, ice crystals near the cloud top absorb solar

253 radiation during daytime and consequently the radiation-induced crystal growth is modulated by

254 solar radiation, which explains the diurnal variation of the PD shown in Figs. 1 and 2 (Zeng et al.,

255 2016). The model also explains the delay of peak of ice cloud mass and coverage, since

256 horizontally oriented ice crystals with larger PD (i.e., flatter) tend to quickly grow into

257 precipitation-sized ones and fall out as precipitation, while ice crystals that are more sphere-like

258 grow slower and stay as ice cloud for a longer time.

259   As for the relationship of AR to particle size, GW17 found its relationship to AR is quite

260 complicated and nonlinear using a fully polarized RTM simulation (see Fig. 9 in GW17). GW17

261 found that the ice crystal with "column" shape overall matched the best with the observations,

262 and the curvature of the PD-TB curve rises with the effective radius, But for certain other shapes,

263 such as rosette with 7 branches, simulation results do not show the clear linear relationship

264 between PD_{peak} and effective radius. Therefore, one cannot rush to the conclusion that the

265 particle size growth exhibits a diurnal cycle. Other factors might also contribute to the diurnal

266 variation of PD but are likely secondary (e.g., liquid cloud that can damp the PD and TB signals

267 also exhibit its own diurnal cycle).

268   The 100% horizontal alignment is unlikely to occur in reality, and the mixing of different ice

269 particle shapes may also vary diurnally. The better-mixed the shapes are (i.e., more percentage of

270 random-orientation), the smaller the AR value is because AR is expected to vanish for the

271 extreme situation of 100% random orientation. If the percentage of randomly oriented particles is

272 the only or major contributor to the diurnal variation of PD_{peak}, then it indicates that along with

273 the growth of deep convective systems from late morning to the early evening, ice particles also

274 tend to become more and more randomly oriented. This makes sense as the vertical motion in

275 deep convective cores tends to generate and maintain a more turbulent environment than that in

276   the ambient environment of the anvils and cirrus. However, this could not explain the ~ 2 hrs

277   delay of the peak/trough of the diurnal cycles of ice cloud mass and coverage. Also, as indicated

278   in the Appendix A, the PD_{peak} information indeed mostly comes from the differentiation of τ_V

279   and τ_H for anvils, instead of from deep convective clouds as 166 GHz quickly saturates at the top

280   several kilometers of the deep convective core. Therefore, the degree of turbulence, or

281   randomness, inside the deep convective cloud is not a major contributor to the value of AR or

282   PD_{peak}.

283

284   **4. Conclusions**

285   High-frequency passive microwave measurements, such as GMI 166 GHz channel, are

286   sensitive to ice cloud scattering. Vertically and horizontally polarized microwave observations

287   are found to differ in cloudy-sky because of the disparity of their optical thicknesses through an

288   ice cloud layer with anisotropic bulk microphysical properties. As a result, the polarimetric

289   radiance difference, or PD, can be used to infer cloud microphysical properties (i.e., ice crystal

290   shape, size, and orientation).

291   The GPM precession orbit provides a valuable chance to study the diurnal variations of PD at

292   166 GHz in the tropics for the first time. The PD-TB relationship bears with a bottom-up bell

293   curve that was investigated extensively in an earlier study of Gong and Wu [2017]. All bell

294   curves can be represented by the peak PD amplitude, called PD_{peak}, which serves as a good

295   measure to characterize the diurnal variation of the PD-TB curve. Similar to other macrophysical

296   quantities like the area of coverage, occurring frequency, and total mass of ice clouds, PD_{peak} is

297   found to vary by only 6% over tropical ocean, but vary dramatically (~ 38%) over tropical land.

298   The maximum and minimum of PD_{peak} occur at local morning and afternoon over tropical land,

299   which lead the diurnal cycle of ice cloud mass and coverage by ~ 2 hrs with an opposite sign.

300   The observed diurnal variation of the PD-TB relationship can be explained quantitatively

301   using a set of different AR values, because AR reflects a bulk effect of ice crystal shape and size

302   in radiative transfer, and the diurnal variation in PD is linked directly to a variation in AR. Other

303   microphysical properties, however, may also play a role in altering the PD-TB relationship as

304   observed and need to be explored with more observations and accurate model representations of

305   ice microphysical properties. Since radiation impacts ice crystal growth via crystal surface

306   temperature (e.g., Zeng, 2008; Zeng et al., 2016), it can subsequently change AR, which in turn

307   changes PD. Although we cannot fully understand the delay and anticorrelation of cloud mass

308   and coverage with respect to PD, the delayed occurrence of ice cloud macro-physical properties

309   indicates the importance of ice microphysics in formation/decay of ice clouds. It is imperative to

310   include these processes in models to replicate the realistic cloud diurnal cycle and its radiative

311   and hydrological effects.

312   This study exemplifies the power of passive microwave polarimetry in remotely sensing

313   ice cloud microphysical properties. The 166 GHz is the highest frequency of polarized channels

314   in GMI. Because ice cloud scattering is more significant at high frequencies, careful fusion of

315   observations from multi-frequency polarized microwave/IR channels makes it feasible to infer

316   both bulk ice particle size and shape simultaneously and allows global studies of ice cloud

317   microphysics on diurnal, seasonal, and interannual time scales. Although it has been well known

318   that ice microphysics are strongly tied together with the evolution of ice cloud macro-properties,

319   this work identifies that understanding the variations in ice microphysics are necessary to predict,

320   infer, and model the bulk properties of the ice clouds and their broader evolution (e.g.,

321   precipitation process). This study is a good exercise to manifest that new satellite

322   instrumentation (e.g., GMI) with novel observational techniques (e.g., paired high-frequency

323   microwave channels) may offer a valuable means to observe and understand the entire cloud-

324   precipitation processes.

325

326   **Appendix A: Where does the PD_{peak} come from?**

327   In Gong and Wu (2017), the bottom-up bell curves of the PD-TB relationship from 89, 166,

328   and 640 GHz observations are explained by the different penetration depth of V-pol and H-pol

329   measurements through an ice cloud layer consisting of horizontally oriented nonspherical ice

330   crystals. In this appendix, we present additional evidence to support this explanation. More

331   importantly, this exercise answers directly to the types of ice cloud, their vertical levels, and how

332   they contribute to the largest PD signal (PD_{peak}).

333   Two years (2014–2015) of collocated CloudSat-GMI data are compiled together to composite

334   the Contoured Frequency by Altitude Diagram (CFAD) in Fig. A1b for the clouds that satisfy the

335   criteria such that $7 K < PD < 20 K$ and $160 K < TBv < 220 K$ (enclosed by the red rectangle box

336   in Fig. A1a). This dataset is produced by Dr. Joe Turk at the Jet Propulsion Lab and details about

337   this dataset can be found in Turk [2017]. To generate robust statistics, we employed two years of

338   data since collocated GPM-CloudSat scenes are sparse. For CloudSat, 0 dBZ roughly separates

339   the thin ice clouds (anvils, cirrus) with low reflectivity from thick ice clouds (thick anvils, deep

340   convective cores) with high reflectivity.

341   As shown in CFADs for V-pol and H-pol, the largest disparity comes from clouds with

342   reflectivity below 0 dBZ and height above 10 km. These clouds are apparently thin anvils (that at

343   least 166 GHz V-pol can partially penetrate through) and cirrus clouds. When the ice cloud

344 becomes thicker and lower, 166 GHz passive microwave observations quickly saturates, and

345 although 166 GHz are still sensitive to these clouds (down to cloud height as low as 2 km and as

346 strong as 25 dBZ), the PD of 166 GHz no longer shows the disparity.

347   One possible explanation of the curvature of the PD-TB relationship that is proposed in

348 GW17 is that turbulence in deep convective cores likely forces the nonspherical ice crystals to be

349 well mixed (i.e., randomly oriented), in which way the PD eventually vanishes when TB gets

350 cold. This exercise demonstrates that although this mechanism is quite plausible, 166 GHz PD

351 measurements cannot identify the turbulence condition in thick ice clouds and therefore cannot

352 be used to verify such a hypothesized mechanism.

353 **Data Access**

354 GMI Level-1 calibrated radiance data and CloudSat-GPM collocation dataset can be acquired

355 from the Precipitation Processing System's (PPS) FTP server at arthurhou.pps.eosdis.nasa.

356 gov. The radiative transfer model is coded and modified by the authors for this specific study.

357 Interested readers are encouraged to contact the lead author directly for a copy of the model. All

358 data used to make the figures in this manuscript are included in the supplementary materials. A

359 README file illustrates the file format, content, and variable meanings.

360

367

Acknowledgement

References

Boukabara, S. A., Garrett, K., Chen, W. C., Iturbide-Sanchez, F., Grassotti, C., Kongoli, C., Chen, R. Y., Liu, Q. H., Yan, B. H., Weng, F. Z., Ferraro, R., Kleespies, T. J., and Meng, H. (2011), MiRS: An All-Weather 1DVAR Satellite Data Assimilation and Retrieval System. IEEE Transactions on Geoscience and Remote Sensing, 49(9), 3249-3272.

Chung, E. S., Sohn, B. J., Schmetz, J., and Koening, M. (2007), Diurnal variation of upper tropospheric humidity and its relations to convective activities over tropical Africa, Atmos. Chem. Phys., 7, 2489–2502, doi:10.5194/acp-7-2489-2007.

Dai, A. and Trenberth, K. E. (2004), The diurnal cycle and its depiction in the community climate system model, J. Climate, 17, 930–951.

Davis, C. P., D. L. Wu, C. Emde, J. H. Jiang, R. E. Cofield, and R. S. Harwood (2005), Cirrus induced polarization in 122 GHz aura Microwave Limb Sounder radiances, *Geophys. Res. Lett.*, **32**, L14806, doi:10.1029/2005GL022681.

Davis, C. P., Evans, K. F., Buehler, S. A.,Wu, D. L., and Pumphrey, H. C. (2007), 3-D polarised simulations of space-borne passive mm/sub- mm midlatitude cirrus observations: a case study, Atmos. Chem. Phys., 7, 4149–4158, doi:10.5194/acp-7-4149-2007.

Defer, E., V. S. Galligani, C. Prigent, and C. Jimenez (2014), First observations of polarized scattering over ice clouds at close-to-millimeter wavelengths (157 GHz) with MADRAS on board the Megha-Tropiques mission, J. Geophys. Res. Atmos.,119 ,12,301–12,316, doi:10.1002/2014JD022353.

Duncan, D. I., and C. D. Kummerow (2016), A 1DVAR retrieval applied to GMI: Algorithm description, validation, and sensitivities, J. Geophys. Res. Atmos., 121, 7415–7429, doi:10.1002/2016JD024808.

Eriksson, P., B. Rydberg, M. Johnston, D. P. Murtagh, H. Struthers, S. Ferrachat, and U. Lohmann (2010), Diurnal variations of humidity and ice water content in the tropical upper

399   troposphere, Atmos. Chem. Phys., 10, 11519-11533.

400   Fu, Q. and K.-N. Liou (1993), Parameterization of the radiative properties of cirrus clouds, J.
401   Atmos. Sci., 50, 2008-2025.

402   Gong, J. and Wu, D. L. (2014), CloudSat-constrained cloud ice water path and cloud top height
403   retrievals from MHS 157 and 183.3 GHz radiances, Atmos. Meas. Tech., 7, 1873–1890,
404   doi:10.5194/amt- 7-1873-2014.

405   Gong, J. and Wu, D. L. (2017), Microphysical properties of frozen particles inferred from Global
406   Precipitation Measurement (GPM) Microwave Imager (GMI) polarimetric measurements, Atmos.
407   Chem. Phys., 17, 1–17, 2017, doi:10.5194/acp-17-1-2017.

408   GPM X-Cal Working Group (2015), NASA Global Precipitation Measurement Level 1C
409   Algorithms, Version 1.4, https://pps.gsfc.nasa.gov/Documents/L1C_ATBD.pdf.

410   Hartmann, D. L., H. H. Hendon, and R. A. Houze, Jr. (1984), Some implications of the
411   mesoscale circulations in tropical cloud clusters for large-scale dynamics and climate. *J. Atmos.*
412   *Sci.*, **41**, 113-121.
413
414   Hartmann, D. L., J. R. Holton and Q. Fu (2001), The heat balance of the tropical tropopause,
415   cirrus and stratospheric dehydration, Geophys. Res. Lett., 28 (10), 1969-1972.

416   Hartmann, D. L., and Berry, S. E. (2017), The balanced radiative effect of tropical anvil clouds, J.
417   Geophys. Res. Atmos., 122, 5003–5020, doi:10.1002/2017JD026460.

418   Heymsfield, A. J., S. Matrosov, B. Baum (2003), Ice water path – optical depth relationships for
419   cirrus and deep stratiform ice cloud layers, J. Atmos. Sci., 42, 1369 – 1390.

420   Hioki, S., P. Yang, B. A. Baum, S. Platnick, K. G. Meyer, M. D. King, and J. Riedi (2016),
421   degree of ice particle surface roughness inferred from polarimetric observations, Atmos. Chem.
422   Phys., 16, doi: 10.5194/acp-16-7545-2016

423   Homeyer, C. R. and Kumjian, M. R. (2015), Microphysical characteristics of overshooting
424   convection from polarimetric radar observations, J. Atmos. Sci., 72, 870–891.

425   Hong, G., G. Heygster, C. A. M. Rodriguez (2006), Effect of cirrus clouds on the diurnal cycle
426   of tropical deep convective clouds, J. Geophys. Res., 111, D06209, doi: 10.1029/2005JD006208.

427   Hong, Y., G. Liu, J.-L. F. Li (2016), Assessing the Radiative Effects of Global Ice Clouds Based
428   on CloudSat and CALIPSO Measurements, J. Clim., doi: http://dx.doi.org/10.1175/JCLI-D-15-
429   0799.1.
430
431   Hou, A. Y., R. K. Kakar, S. Neeck, A. A. Azarbarzin, C. D. Kummerow, M. Kojima, R. Oki, K.
432   Nakamura, and T. Iguchi (2014), The Global Precipitation Measurement Mission. *Bull. Amer.*
433   *Meteor. Soc.*, **95**, 701–722.
434

435 Jiang, J. H., H. Su, C. Zhai, T. J. Shen, T. Wu, J. Zhang, etc. (2014), Evaluating the diurnal cycle
436 of upper-tropospheric ice clouds in climate models using SMILES observations, J. Atmos. Sci.,
437 72, 1022- 1044, doi: 10.1175/JAS-D-14-0124.1.

439 Kiehl, J. T., J. J. Hack, and B. P. Briegleb (1994), The simulated Earth radiation budget of the
440 National Center for Atmospheric Research Community Climate Model CCM2 and comparisons
441 with the Earth Radiation Budget Experiment (ERBE), J. Geophys. Res.,99 (D10), 20,815–20,827.

442 Liou, K. N., Y. Takano, P. Yang, and Y. Gu (2002), Radiative transfer in cirrus clouds: Light
443 scattering and spectral information, in Cirrus, edited by D. Lynch et al., pp. 265–296, Oxford
444 Univ. Press, New York.

445 Liu, C. and Zipser, E. J. (2008), Diurnal cycles of precipitation, clouds, and lightning in the
446 tropics from 9 years of TRMM observations, Geophys. Res. Lett., 35, L04 819,
447 doi:10.1029/2007GL032437.

448 Millan, L., W. Read, Y. Kasai, A. Lambert, N. Livesey, J. Mendrok, H. Sagawa, T. Sano, M.
449 Shiotani, and D. L. Wu (2013), SMILES ice cloud products, J. Geophys. Res., 118, 6468-6477,
450 doi: 10.1002/jgrd.50322.

451 Prigent, C., J. R. Pardo, M. I. Mishchenko, and W. B. Rossow (2001), Microwave polarized
452 signatures generated within cloud systems: Special Sensor Microwave Imager (SSM/I)
453 observations interpreted with radiative transfer simulations, *J. Geophys. Res.*, 106(D22), 28243–
454 28258.

455 Prigent, C., E. Defer, J. R. Pardo, C. Pearl, W. B. Rossow, and J.-P. Pinty (2005), Relations of
456 polarized scattering signatures observed by the TRMM Microwave Instrument with electrical
457 processes in cloud systems, Geophys. Res. Lett., 32, L04810,Skofronick-Jackson, G. M. and J. R.
458 Wang (2000), The Estimation of Hydrometeor Profiles from Wideband Microwave Observations.
459 *J. Appl. Meteor.*, **39**, 1645–1656.

460 Raymond, D. J. and X. Zeng (2000), Instability and large-scale circulations in a two-column
461 model of the tropical troposphere. *Quart. J. Roy. Meteor. Soc.*, **126**, 3117-3135.

462 Sato, T., H. Miura, M. Satoh, Y. N. Takayabu (2009), Diurnal cycle of precipitation in the
463 tropics simulated in a global cloud-resolving model, J. Clim., doi: 10.1175/2009JCLI2890.1.

464 Skofronick-Jackson, G. and Coauthors (2015), Global Precipitation Measurement Cold Season
465 Precipitation Experiment (GCPEX): For Measurement's Sake, Let It Snow. *Bull. Amer. Meteor.*
466 *Soc.*, **96**, 1719–1741.

467 Soden, B. J. (2000), The diurnal cycle of convection, clouds, and water vapor in the tropical
468 upper troposphere, Geophys. Res. Lett., 27, 2173–2176.

469 Tang, G., R. L. Panetta, P. Yang, G. W. Kattawar, P.-W. Zhai (2017), Effect of ice crystal
470 surface roughness and air bubble inclusions on cirrus cloud radiative properties from remote
471 sensing perspective, J. Quan. Spec. Rad. Trans., 195, 119-131, doi: 10.1016/j.jqsrt.2017.01.016.

472 Tian, B., Soden, B. J., and Wu, X. (2004), Diurnal cycle of convection, clouds, and water vapor
473 in the tropical upper troposphere: Satel- lites versus a general circulation model, J. Geophys. Res.,
474 109, D10101, doi:10.1029/2003JD004117.

475 Turk, J. (2017), CloudSat-GPM Coincidence Dataset, Version 2A,
476 https://pps.gsfc.nasa.gov/Documents/CSATGPM_COIN_ATBD.pdf

477 Waliser, D. E., Li, J.-L. F., Woods, C. P., Austin, R. T., Bacmeister, J., Chern, J., Genio, A. D.,
478 Jiang, J. H., Kuang, Z., Meng, H., Minnis, P., Platnick, S., Rossow, W. B., Stephens, G. L., Sun-
479 Mack, S., Tao, W.-K., Tompkins, A. M., Vane, D. G., Walker, C., and Wu, D. (2009), Cloud ice:
480 a climate model challenge with signs and expectations of progress, J. Geophys. Res., 114,
481 D00A21, doi:10.1029/2008JD010015.

482 Yang, G.-Y., and J. Slingo (2001), The diurnal cycle in the tropics, Mon. Weather Rev., 129,
483 784–801.

484 Zeng, X. (2008), The influence of radiation on ice crystal spectrum in the upper troposphere.
485 *Quart. J. Roy. Meteor. Soc.*, **134**, 609-620.

486 Zeng, X., W.-K. Tao, M. Zhang, A. Y. Hou, S. Xie, S. Lang, X. Li, D. Starr, and X. Li (2009a),
487 A contribution by ice nuclei to global warming. Quart. J. Roy. Meteor. Soc., 135, 1614-1629.

488 Zeng, X., W.-K. Tao, M. Zhang, A. Y. Hou, S. Xie, S. Lang, X. Li, D. Starr, X. Li, and J.
489 Simpson, (2009b), An indirect effect of ice nuclei on atmospheric radiation. J. Atmos. Sci., 66,
490 41-61.

491 Zeng, X., G. Skofronick-Jackson, L. Tian, A. E. Emory, W. S. Olson and R. A. Kroodsma (2016),
492 Analysis of the GMI/CoSMIR microwave polarization data for ice crystal modeling. The 2016
493 Precipitation Measurement Mission (PMM) meeting, Houston, Texas, Oct. 24-28, 2016.

494 Zhou, C., Yang, P., Dessler, A. E., Hu, Y., & Baum, B. A. (2012), Study of horizontally oriented
495 ice crystals with CALIPSO observations and comparison with Monte Carlo radiative transfer
496 simulations. *Journal of Applied Meteorology and Climatology*, *51*(7), 1426-1439.

497

498 *Figure Titles:*

499 *Figure 1: PD-TBv curves at different local solar times (colors) over tropical ocean (a) and land*

500 *(b). A curve is a simple connection of the mean values at each TB bin of the 2D PDF integrated*

501 *from year 2015 of GMI observations at 166 GHz between 30˚S and 30˚N. The black dash lines*

502 *indicate the 3σ threshold for computing the cloud occurring frequency and mean TB, and dash-*

503 *dot lines exhibit the threshold for describing the PD-TB relationship.*

504 *Figure 2: Top: time series of the mean PD value for clouds with TB in the range of [180, 210] K*

505 *(black), mean cloud occurring frequency (OF; red), and mean TB (TB$_{cld}$; blue; axis value is*

506 *upside-down to match the physical meaning of total column ice mass) for clouds below the 3σ*

507 *threshold (red) at tropical ocean (a) and land (b) during 2015. Bottom: lag-correlation between*

508   *the time series of PD and OF (red) and PD and TB$_{cld}$ (blue) over ocean (c) and land (d).*
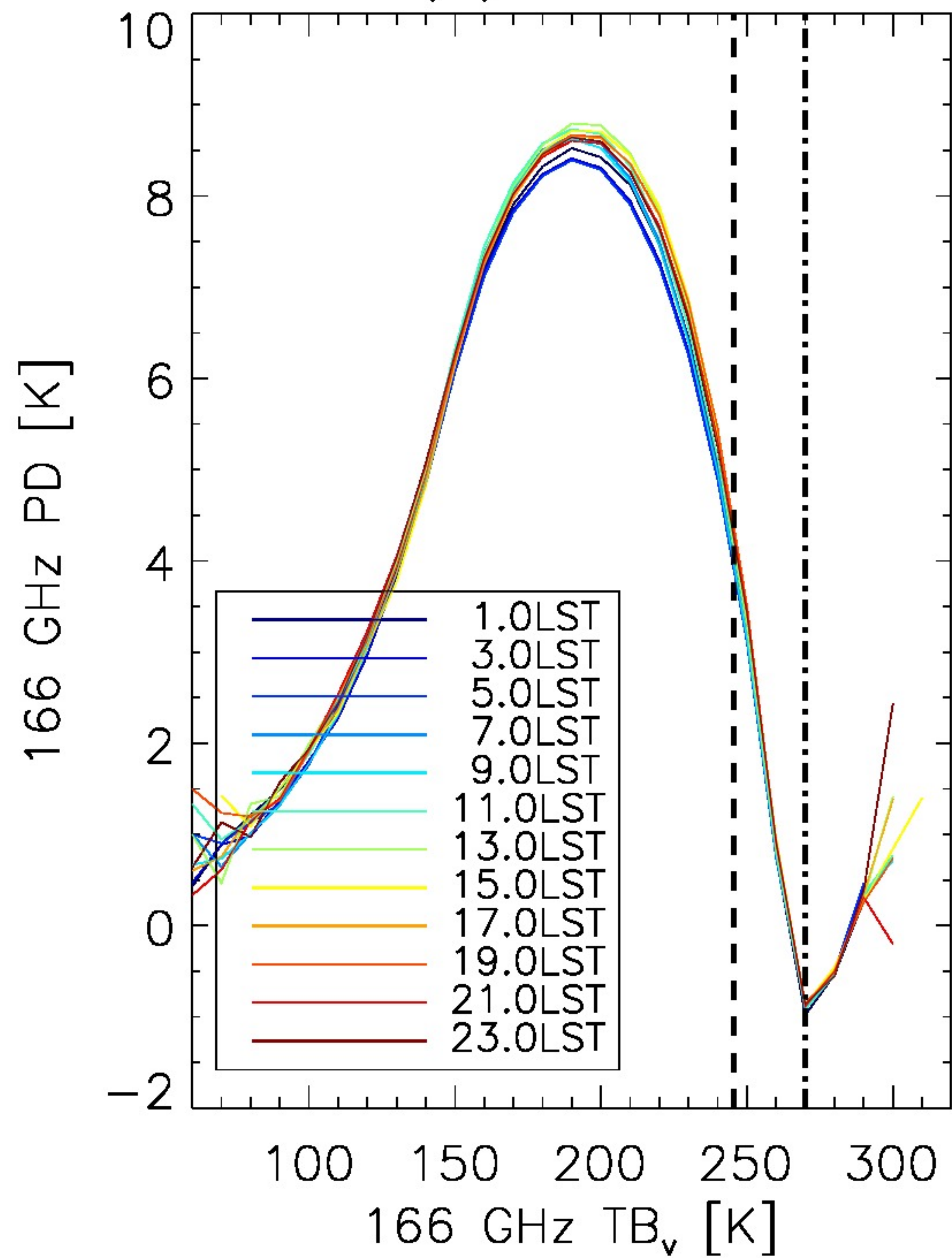
509   *Positive/negative lag time corresponds to a lead/lag of the former time series to the latter ones.*

510   ***Figure 3****: (a) Example of how simulation compares with observations at 166 GHz. The simulated*

511   *166 GHz PD-TBv relationships are shown in black lines with different AR values (AR varies*

512   *from thin to bold between 1.0 and 1.5 with an increment of 0.04); the top of the simulated results*

513   *shows the mean of the observed ensemble for the entire year of 2015 between the equator and*

514   *10°N with the variability shown in pink envelope (adapted from Fig. 8b of Gong and Wu, 2017).*

515   *The best-fit AR values derived from (a) for each time frame are plotted as stars in (b) and (c) for*

516   *ocean and land situations, respectively. Observations are taken from the curves shown in Fig. 1*

517   *and color legend is the same as Fig. 1. See the context for the definition of "best-fit".*

518   ***Figure A1****: (a) Two-dimensional Probability Density Function (PDF) of PD (i.e., ΔTB) and TBv*

519   *derived from GMI 166 GHz oceanic measurements during July 2015 collected between the*

520   *equator and 10°N. This figure is adapted from Fig. 3c of Gong and Wu (2017); (b) CFADs of*

521   *clouds selected from the red rectangle box enclosed area in (a). The black and red contours*

522   *correspond to 166 GHz V-pol and H-pol CFAD, respectively.*
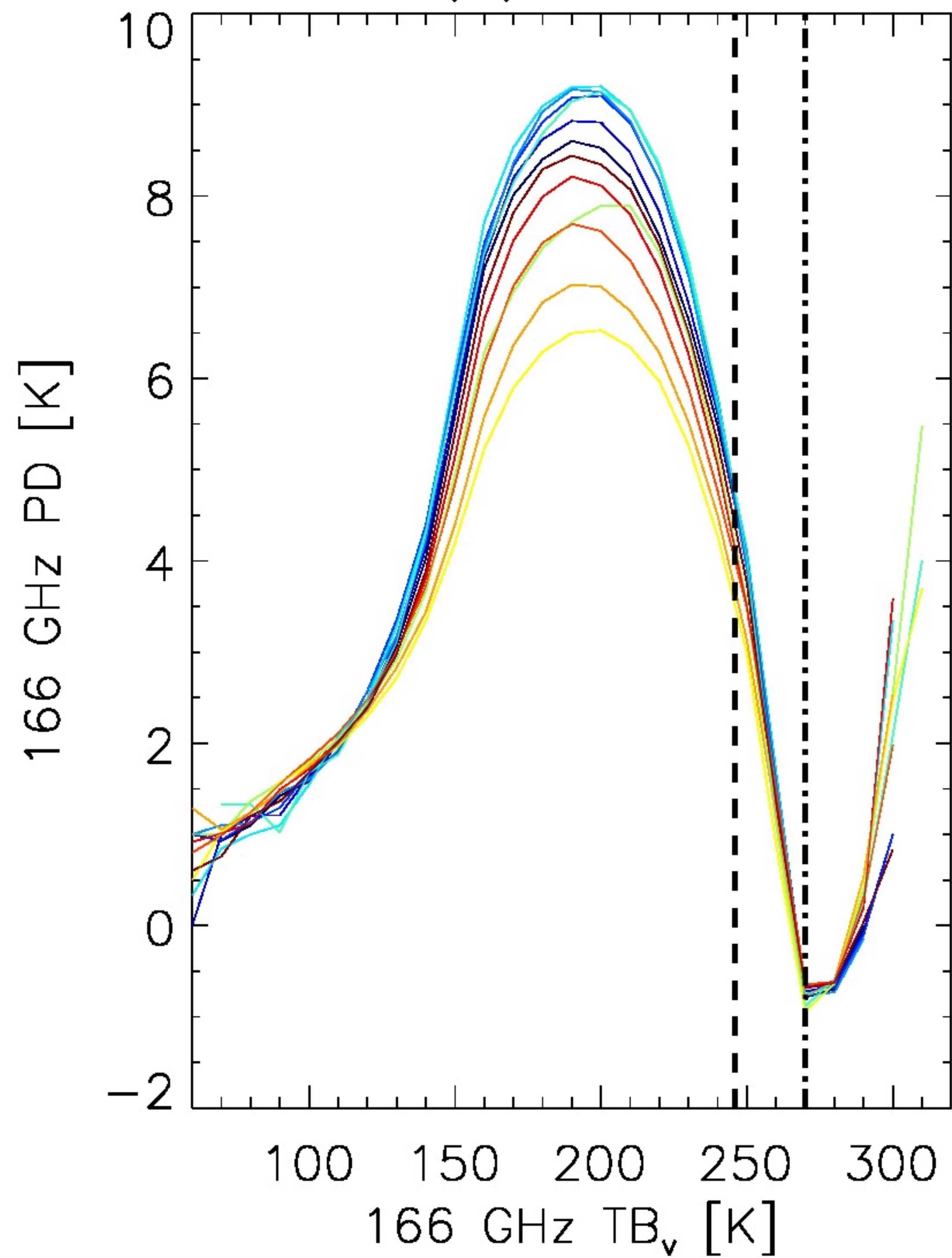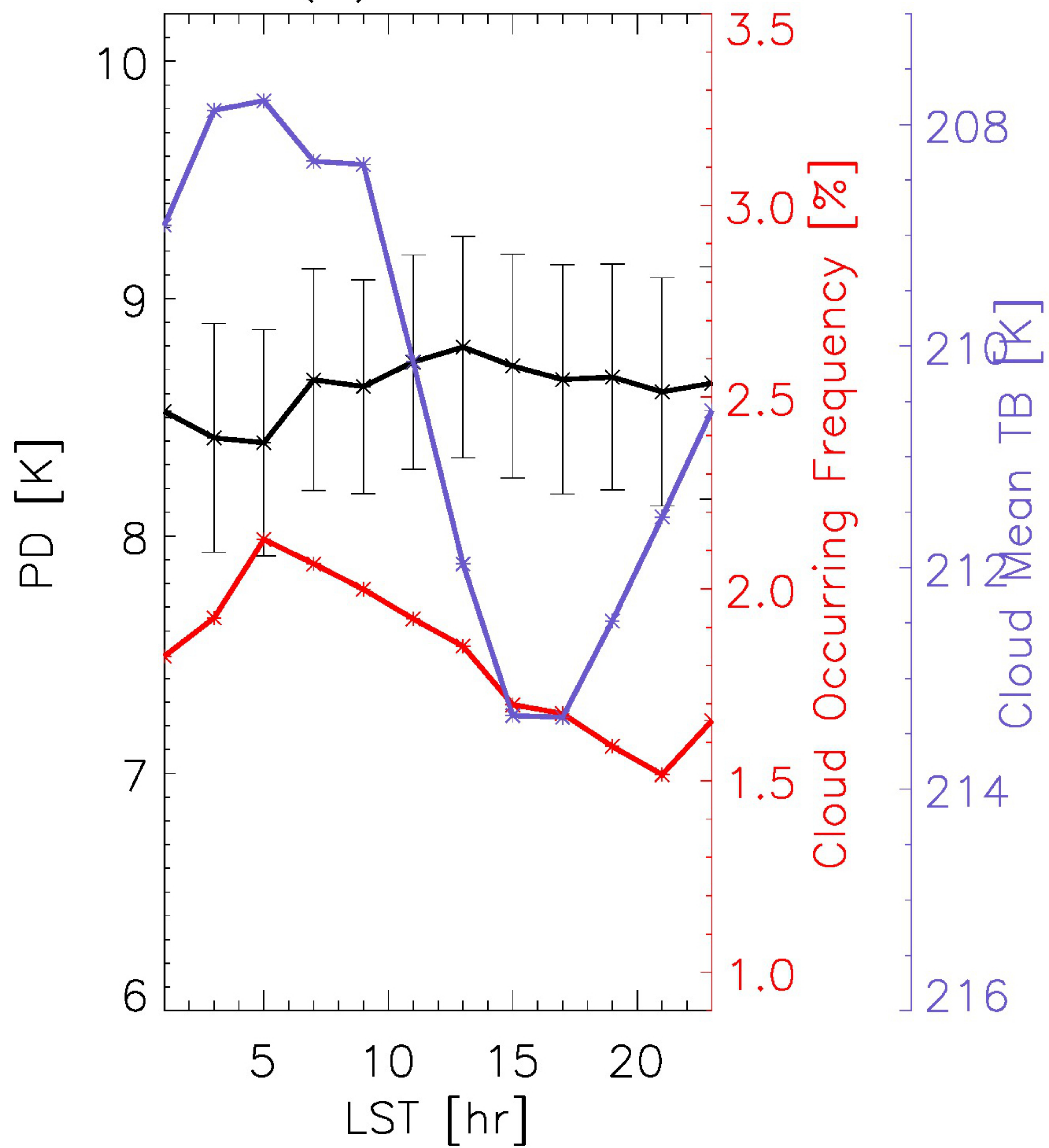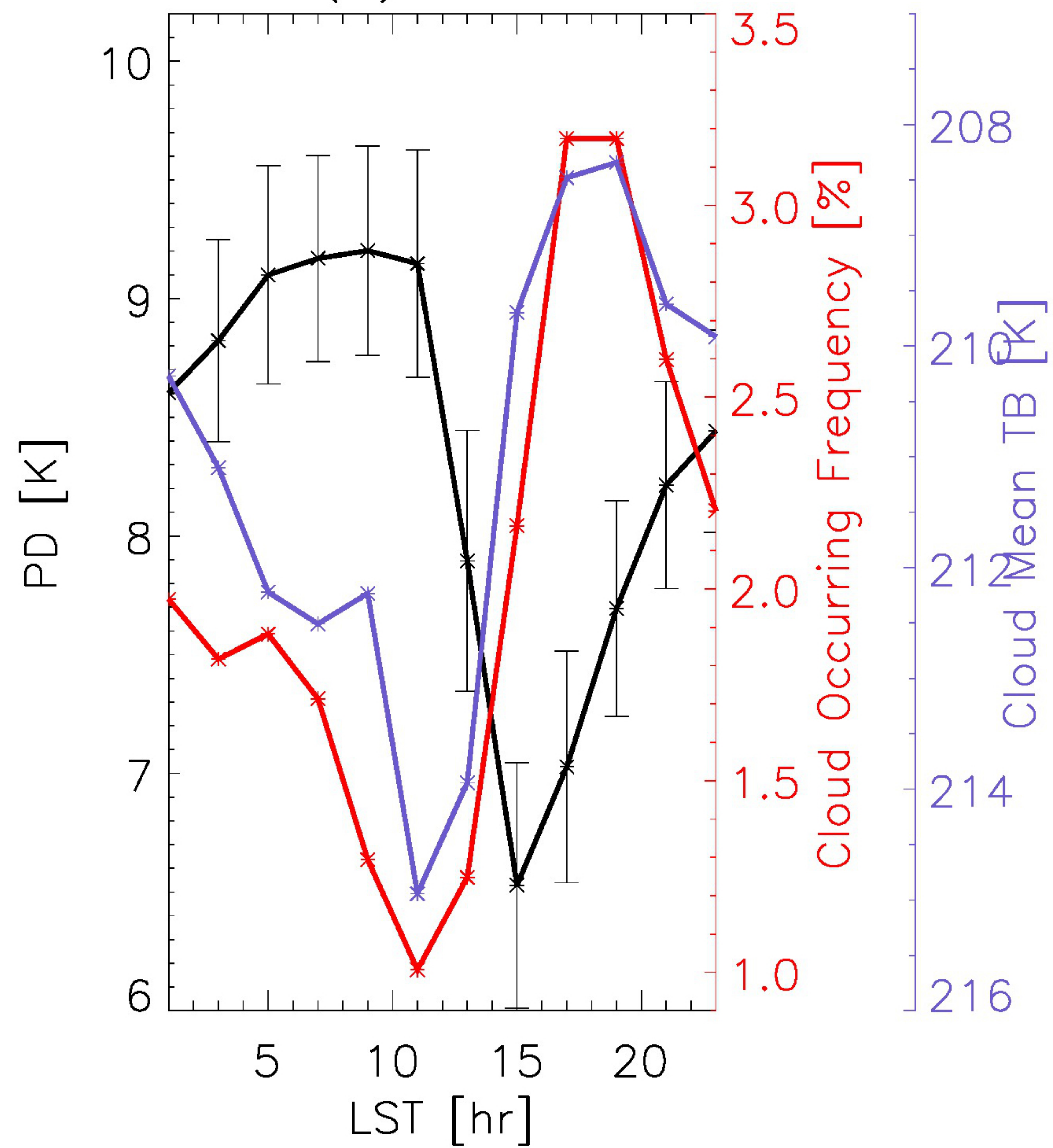
Figure 1.

(a) Ocean   (b) Land

166 GHz PD [K]

166 GHz TB_v [K]

1.0LST
3.0LST
5.0LST
7.0LST
9.0LST
11.0LST
13.0LST
15.0LST
17.0LST
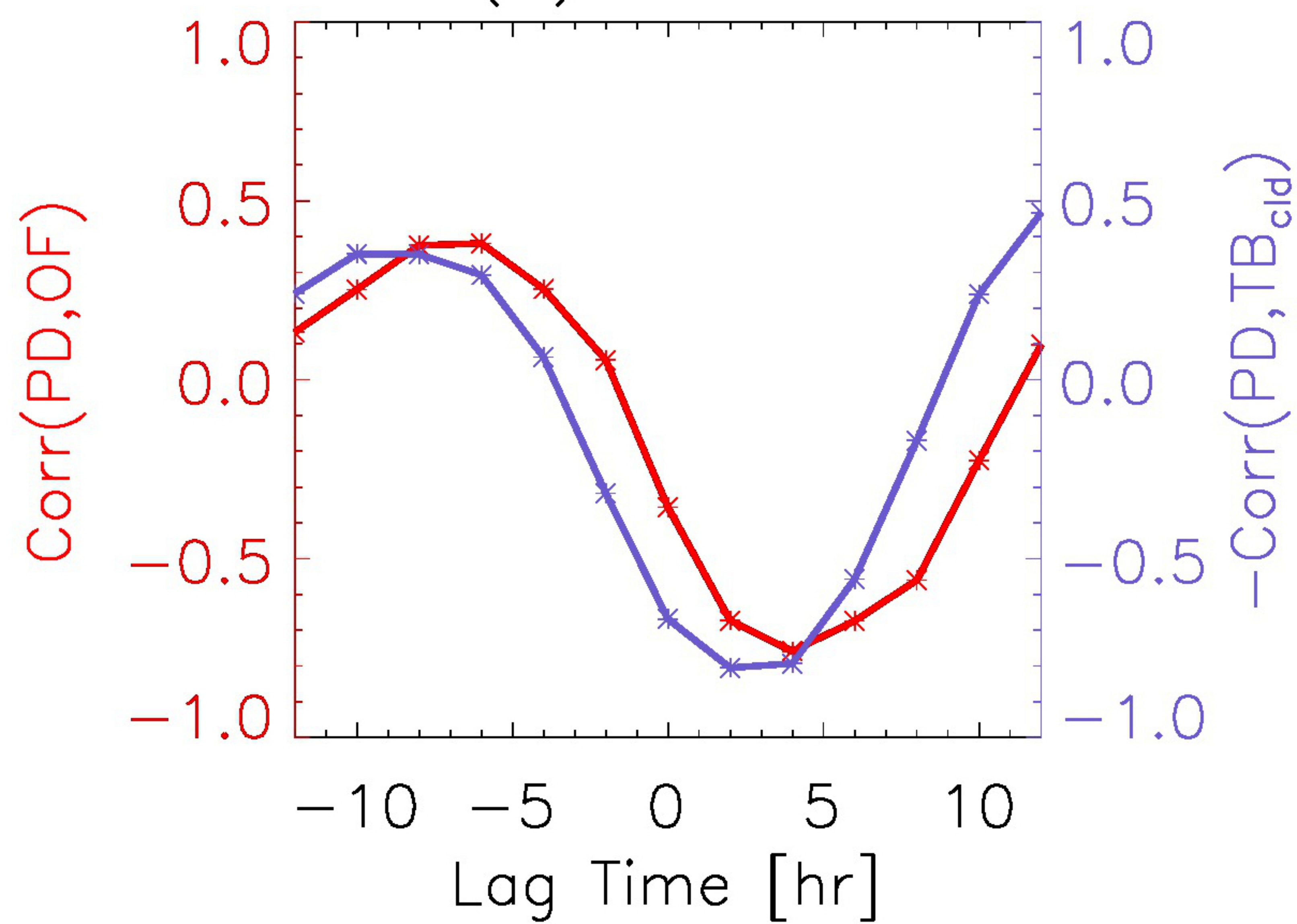19.0LST
21.0LST
23.0LST

Figure 2.

(a) Ocean
(b) Land
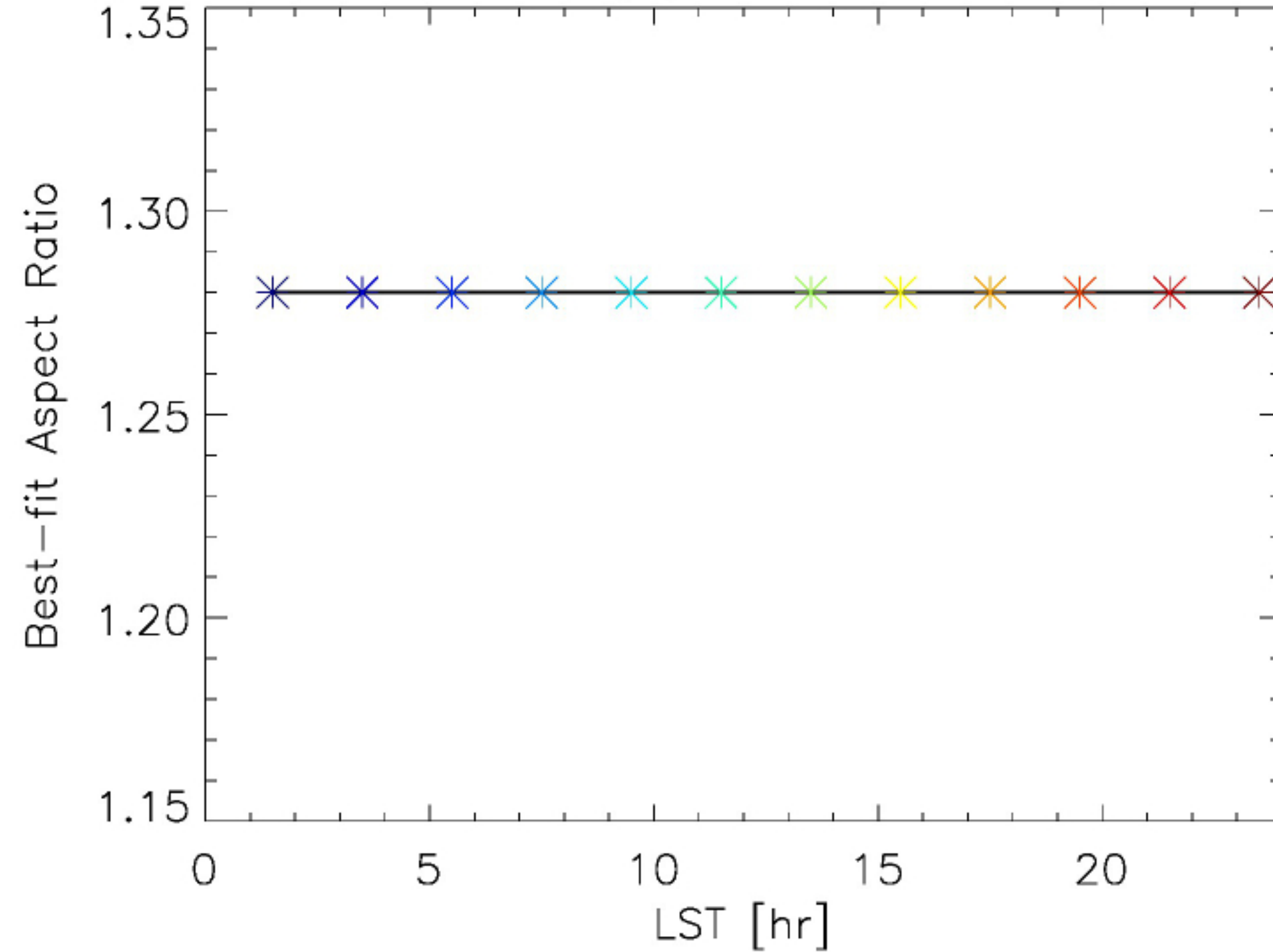(c) Ocean
(d) Land
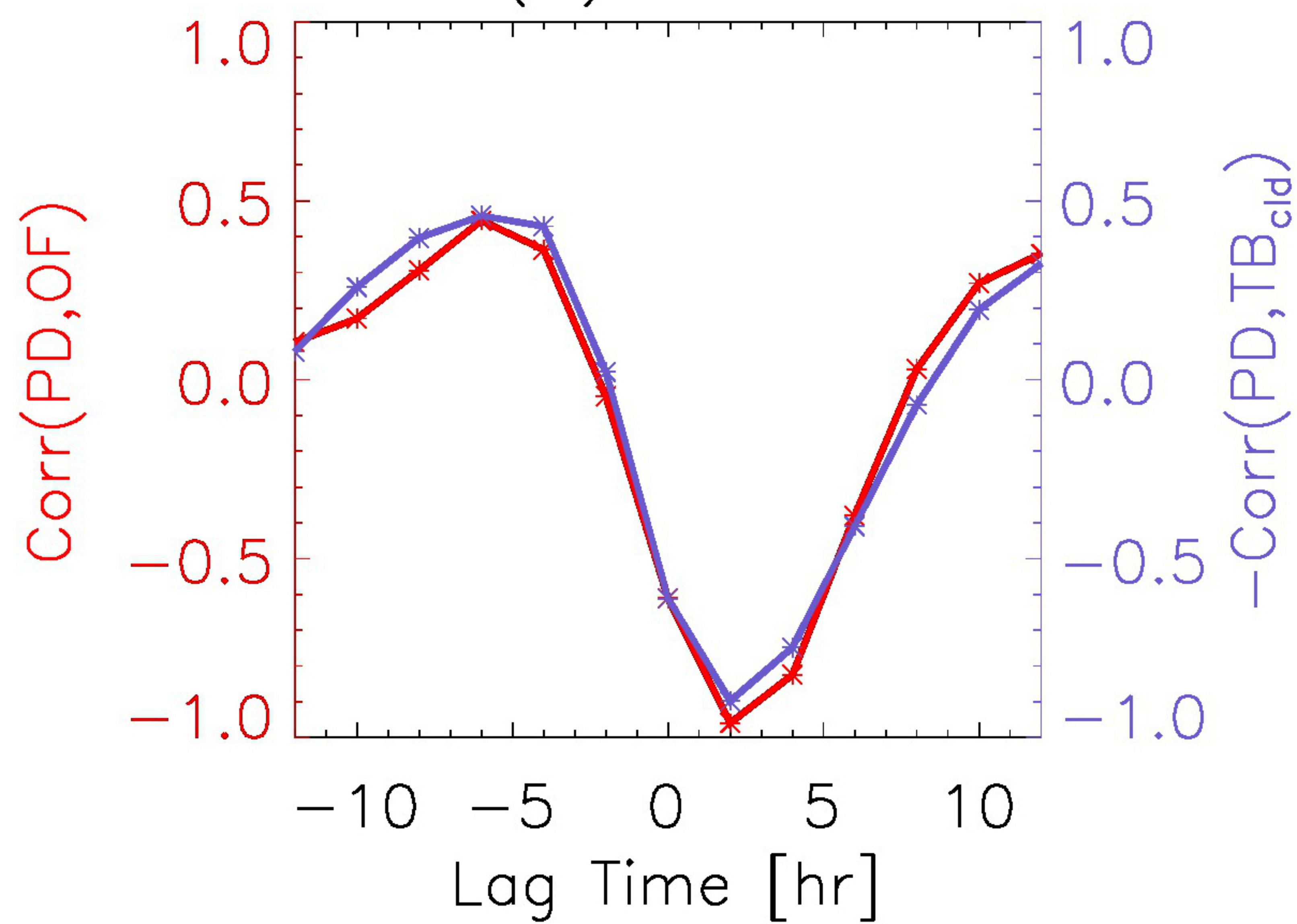
Figure 3.

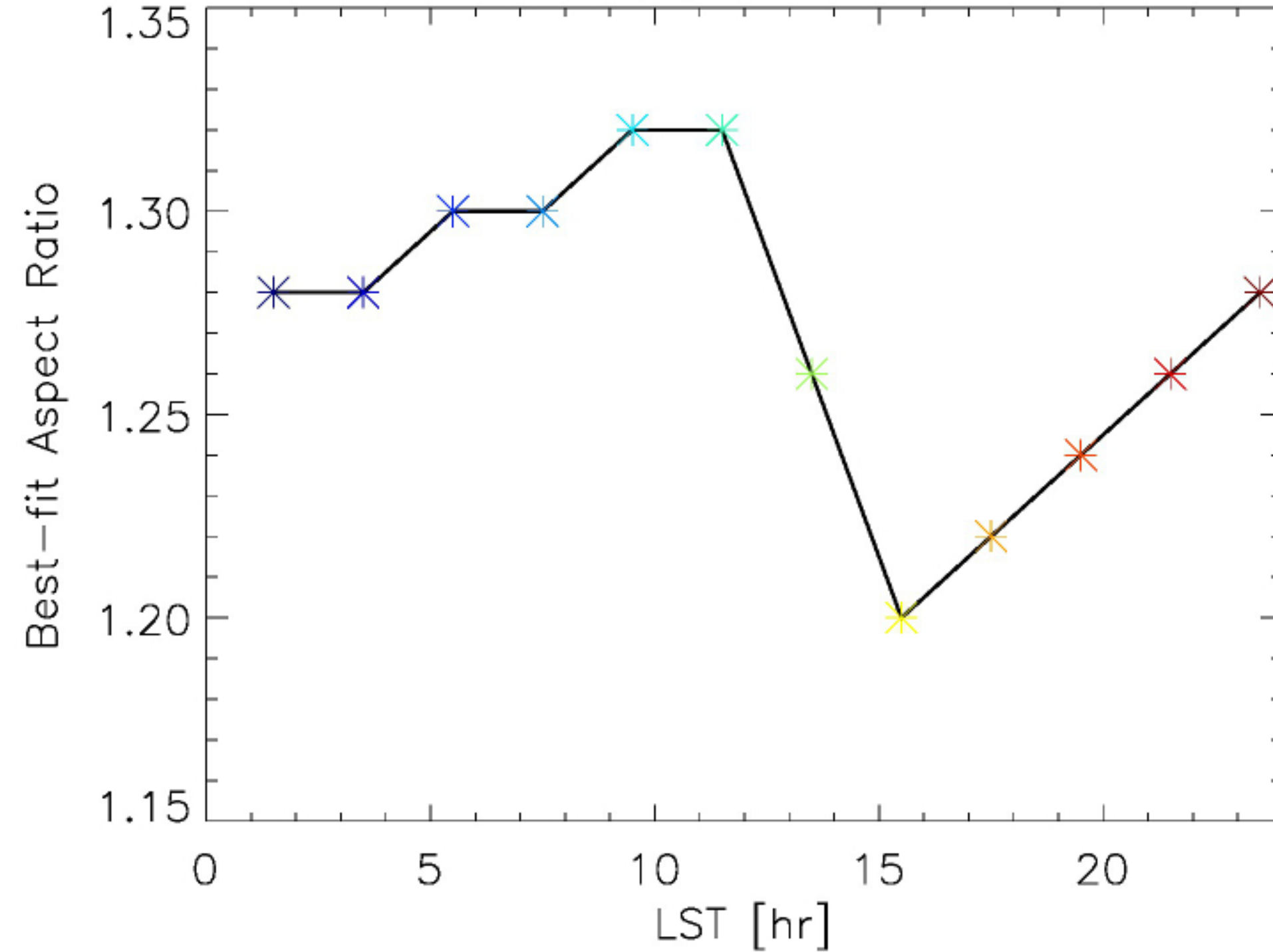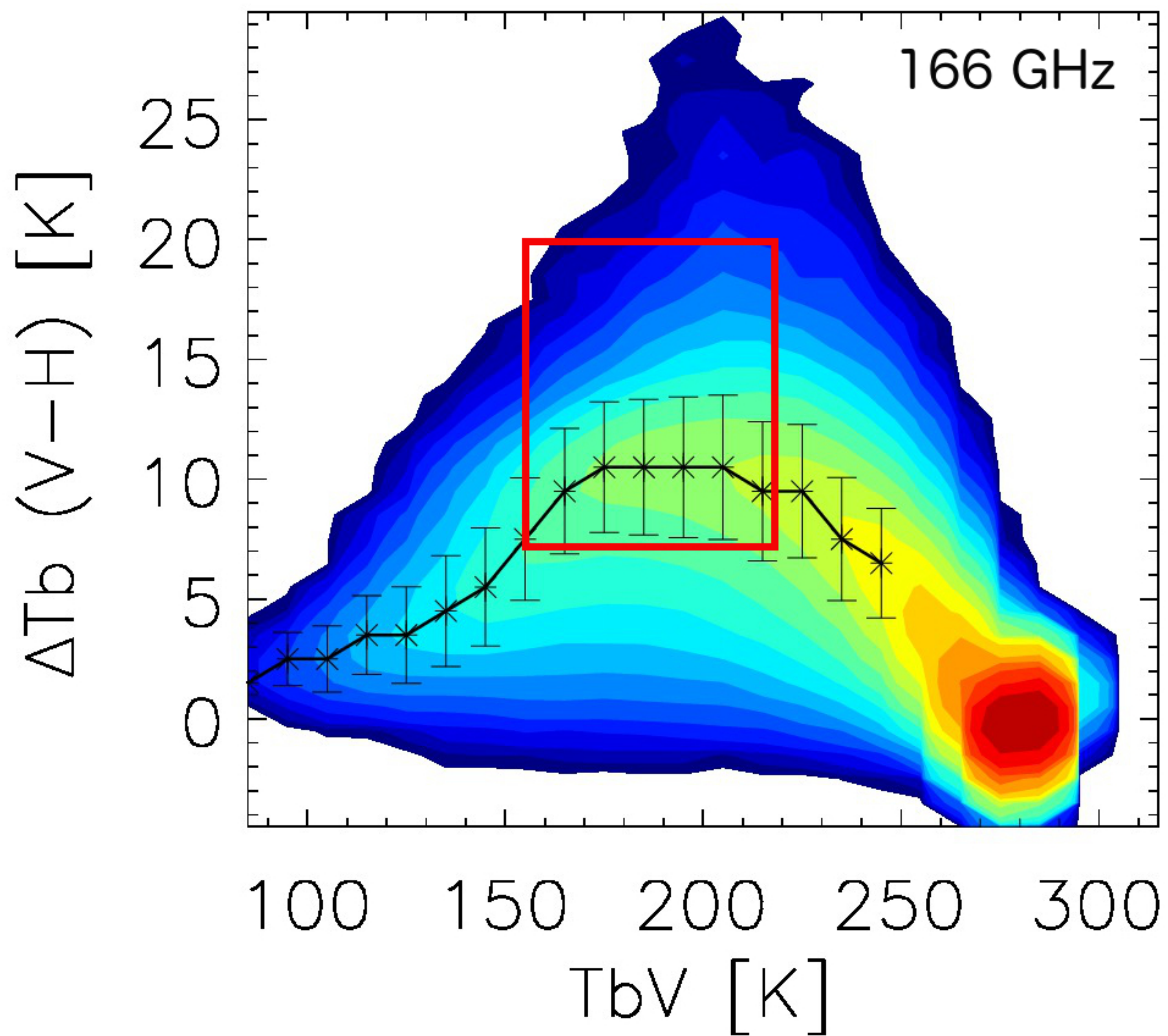**(a) Example of Best-fit**   **(b) Ocean**   **(c) Land**
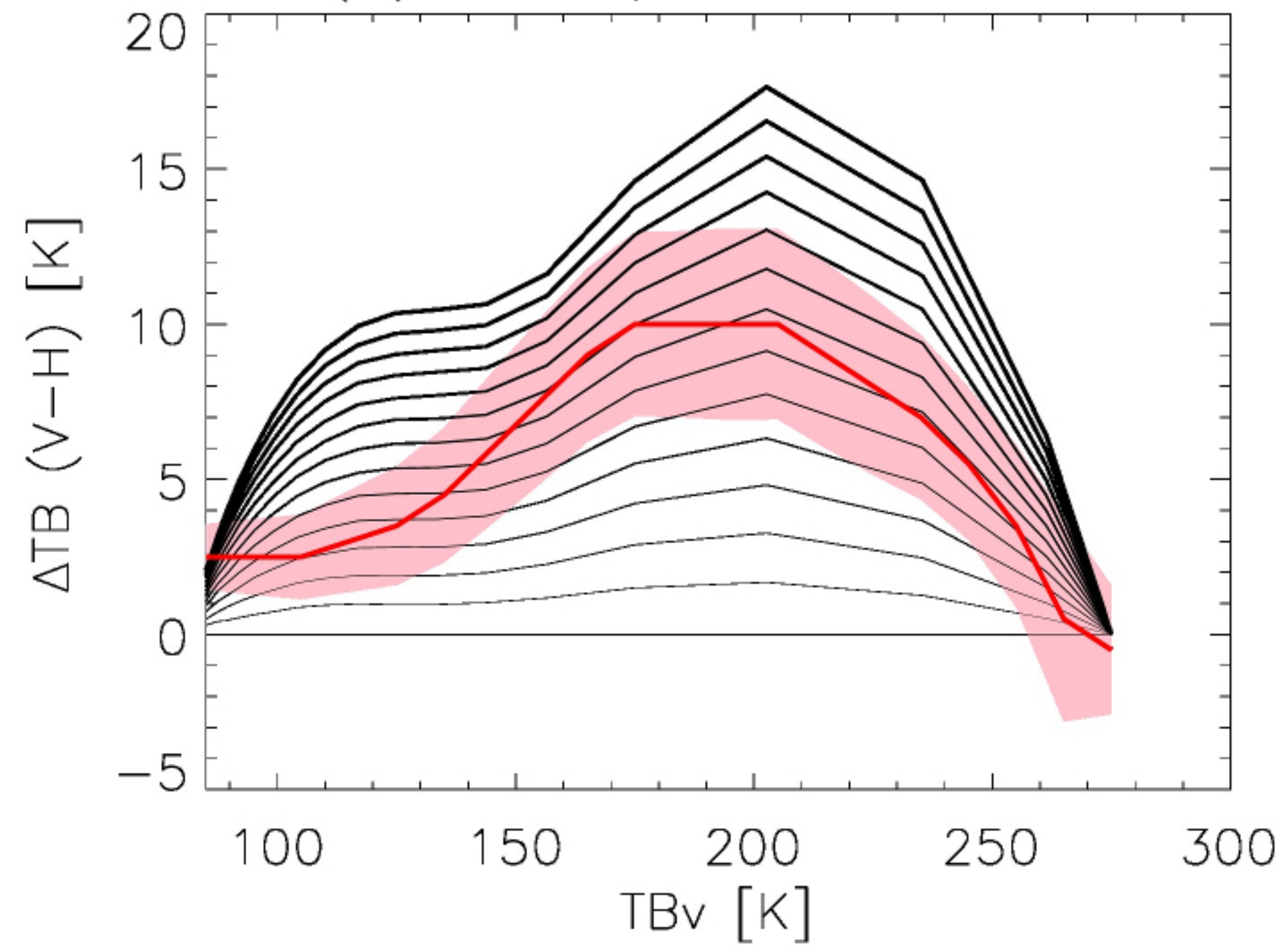
Figure A1.

(a) PDF, Ocean, [0, 10N], July 2015

(b) CFAD, [30S, 30N], 2014-2015

166 GHz

166 GHz, V
166 GHz, H